Investigation of hydrogen embrittlement behavior in X65 pipeline steel under different hydrogen charging conditions

D. Wang [a,*], A.B. Hagen [b], P.U. Fathi [b,c], M. Lin [d], R. Johnsen [a], X. Lu [a]

[a] Department of Mechanical and Industrial Engineering, Norwegian University of Science and Technology (NTNU), 7491, Trondheim, Norway
[b] SINTEF Industry, 7456, Trondheim, Norway
[c] Department of Physics, King's College London, Strand, London, WC2R 2LS, United Kingdom
[d] Department of Structural Engineering, Norwegian University of Science and Technology (NTNU), 7491, Trondheim, Norway

ARTICLE INFO

ABSTRACT

The hydrogen effect on a X65 carbon steel was investigated by tensile tests under both ex-situ and in-situ hydrogen charging conditions. The fractured samples were characterized and compared using a combination of scanning electron microscopy, electron backscattering diffraction, and energy-dispersive spectroscopy. The work highlights that the in-situ hydrogen charging is a necessity for investigation of hydrogen detrimental effects on the studied material, where a pronounced reduction in fracture elongation, the evolution of secondary cracks on gauge surface, and the corresponding brittle fractography were thoroughly characterized after in-situ testing. The reason resides in the rapid hydrogen outgassing effect, which was proved by Fick's law-based diffusion models. Then the interrupted tensile tests were performed to track the crack initiation and propagation behavior. The results show that the majority of cracks initiated at the interfaces of MnS and Al_2O_3 inclusions or between inclusions and matrix, which attributes to the elevated stress concentration around the inclusions. Moreover, the cracks were found to propagate along the {110} slip planes.

1. Introduction

Today, global warming is influencing our daily life from frequent natural disasters to inadequate food supply. The main reason for the climate change is the excess emission of greenhouse gases, mostly carbon dioxide and methane, from burning of fossil fuels. Therefore, the energy transition from traditional oil and gas to clean and renewable energy is imperative. Hydrogen, with high energy efficiency and overwhelming environmental benefits [1,2], is attracting attention as a promising candidate for the future energy provider. In fact, an increasing number of pipelines that were designed to transport oil and gas are being investigated to be used to deliver compressed hydrogen gas. However, despite the massive advantages of hydrogen energy, severe mechanical degradation can be expected on metallic structural materials when exposed to hydrogen-rich environments, known as hydrogen embrittlement [3,4]. The hydrogen embrittlement describes a fracture transition from ductile mode in hydrogen-free condition to hydrogen-induced brittle failure, leading to an unpredictable failure of the structural component. Therefore, the effect of hydrogen on the pipeline steels needs to be carefully evaluated before hydrogen gas

transportation, ensuring a safe and efficient application.

Ever since the first-time description on hydrogen detrimental effect in pure iron in the early 1870s [3], intensive research has been carried out to explain and reveal the intrinsic hydrogen behavior on metallic materials. Till date, the hydrogen-enhanced decohesion (HEDE) [5,6], hydrogen-enhanced localized plasticity (HELP) [7–10], and hydrogen-enhanced strain-induced vacancy formation (HESIV) [11–14] are the most invoked mechanisms. The HEDE mechanism proposes a hydrogen-reduced cohesive energy of atomic bonding, resulting in cleavage or intergranular fracture under excessive applied stress. According to HELP mechanism, the mobility of dislocation is enhanced by hydrogen due to its shielding effect on dislocation elastic field, results in slip localization with crack initiation. The HESIV model suggests that hydrogen can promote the formation of vacancy, which coalesce and combine to larger voids, enhancing crack growth. Despite the intensive studies on the mechanism, it has been widely accepted that hydrogen embrittlement is a complex phenomenon, which is determined by multiple factors including the sources of hydrogen, material microstructures and testing approaches. As a result, none of the mechanisms introduced above can exclusively explain all hydrogen degradation

---

behavior. Moreover, a synthesis of different mechanisms is often invoked to describe complex embrittlement phenomena [15,16].

Carbon steels are widely used as material for long-distance pipeline systems owning to their combinations of good weldability, superior mechanical properties, and relatively low cost [17,18]. Given the potential use for hydrogen transportation, the hydrogen embrittlement is a crucial safe issue for applications. In fact, the hydrogen effect on carbon steels has been intensively studied for decades. Specifically, different types of stress states, e.g., tensile test [19–21], fatigue test [22,23], and nanoindentation test [24], have been carried out to evaluate the hydrogen degradation effect at multi-scale levels. Also, different hydrogen sources from electrochemical charging [19,25] or high-pressure hydrogen gas [20,26] have been adopted and compared. Furthermore, the effect of different carbon steel grades [20,27] and heat treatment [28] on the susceptibility to hydrogen embrittlement have been examined and documented. In addition, the damage in the form of blisters and cracks caused by hydrogen charging has been reported on X65 and X80 steels [29,30]. Overall, the hydrogen shows a detrimental effect on the mechanical properties of carbon steels. However, carbon steels are generally composed of a mixture of micro constituents including ferrite, bainite, perlite, or martensite that significantly differ in volume fraction with uneven distribution. The non-metallic inclusions rich in phosphorus, sulfur, manganese, and aluminum have also been widely reported with varying shape, chemical composition, and distribution [31,32]. Such complex microstructure makes the susceptibility of carbon steels to hydrogen embrittlement on a case-by-case basis. Moreover, both ex-situ and in-situ hydrogen charging methods have been adopted to study the hydrogen embrittlement on carbon steels [33–35]. The ex-situ pre-charging method enables real-time observation of the tensile process by electron/optical microscopy [33]. However, the hydrogen outgassing during the test results in an uneven hydrogen distribution, making it challenging to connect the observed effect with a quantified hydrogen content. On the other hand, the in-situ charging method ensures an evenly distributed hydrogen with a constant hydrogen content in the sample, the drawbacks mentioned above from ex-situ charging can be avoided.

In this study, the different hydrogen charging methods, i.e., ex-situ charging and in-situ charging, were first performed to find out a proper charging approach for the studied X65 carbon steel. Then the interrupted tensile tests were carried out with a particular focus on the crack initiation and propagation behavior, finding the "vulnerable spot" and providing a fundamental understanding of the degradation mechanism of the material under hydrogen attack.

2. Experimental

2.1. Materials and sample preparation

In this work, a commercial X65 grade carbon steel was studied. The nominal composition of the material is listed in Table 1. The steel received from the supplier is a pipe-wall with 15.4 mm thickness. The pipe was first austenitized in a gas fired walking beam furnace at 910 °C followed by water quenching, then a tempering process was conducted with a target temperature of 655 °C. The samples used for the tensile tests were from the middle area of the pipe along the longitudinal direction. The samples were cut by electrical discharge machining into a two-step dog-bone shape with a gauge geometry of 5 mm × 2 mm × ∼1 mm as shown in Fig. 1. The relative long dimension of the clamping part

for sample shown in Fig. 1b was specially designed for mounting the in-situ charging setup as shown in Fig. 1c. Prior to the hydrogen charging and tensile test, the sample surface was mechanically ground till 4000 grit SiC paper followed by fine polishing processes with 3 μm and 1 μm diamond pastes. Then OPS polishing was carried out using 40 nm colloidal silica suspension for 15 min to remove the deformation layer from the mechanical polishing.

2.2. Ex-situ and in-situ tensile test

The tensile tests in this study were carried out by a Kammrath & Weiss tensile/compression module. The tests were performed at ambient temperature in three different conditions: vacuum condition inside scanning electron microscope (SEM) chamber (4.7E-3 Pa) for in-situ observation, air condition, and in-situ hydrogen charging condition. For the vacuum condition, a strain rate of 10^{-4} s^{-1} was applied. For the air condition, a faster strain rate of 10^{-3} s^{-1} was adopted. In these two testing groups, both hydrogen-free and hydrogen pre-charged samples were tested. Regarding the in-situ hydrogen charging tests, both the 10^{-4} s^{-1} and 10^{-3} s^{-1} strain rates were applied. For each testing condition, two parallel tests were performed to guarantee a reproducible result. A detailed explanation about the experimental design will be discussed in the discussion section. The electrolyte for hydrogen charging was a glycerol-based electrolyte, consisting of 600 g borax (sodium tetraborate decahydrate) dissolved into 1 L glycerol, which was further diluted by 20 vol% distilled water with 0.002 M $Na_2S_2O_3$ to enhance the hydrogen uptake. The applied electrolyte can preserve the sample surface from corrosion during electrochemical hydrogen charging, easing the following characterization without extra surface preparation [36,37]. The pre-charging process was performed with a constant current density of −5 mA/cm^2 for 12 h. After the charging, the tensile tests were started within 5 and 10 min in air and vacuum conditions, respectively. Regarding the test with in-situ hydrogen charging, the samples were first pre-charged for 3 h before starting the test. Then the charging was continuously applied during the whole tensile test. The interrupted tensile tests were also performed under the in-situ condition until Ultimate Tensile Strength (UTS). Meanwhile, further straining with step of 2% strain was applied to trace the secondary crack initiation and propagation. A detailed summary of the different testing conditions is presented in Table 2.

2.3. Characterization

Prior to the hydrogen charging and mechanical testing, the microstructure of the studied X65 carbon steel was characterized by SEM (Quanta 650, Thermo Fisher Scientific Inc., US) equipped with a backscattered electron (BSE) detector, electron backscatter diffraction (EBSD), and electron channeling contrast imaging (ECCI) techniques. Regarding the tensile tests in vacuum condition, the in-situ SEM observation was performed through the test, recording the fracture behavior. After loading to fracture, the fractography and gauge surface were characterized using SEM. In addition, the surface secondary cracks from interrupted tests were analyzed by EBSD techniques with an accelerating voltage of 20 kV and a step size of 0.1 μm. For the EBSD analysis on secondary cracks, the fractured sample surface was reprepared to the OPS level to obtain a clear diffraction pattern.

2.4. Hydrogen content

To determine the amount of hydrogen in different testing conditions and thus discuss the influence of hydrogen content on the mechanical degradation, the hot extraction test was performed on the charged samples. The hot extraction test was conducted using Bruker G4 PHOENIX DH with a mass spectrometry detector (ESD 100, InProcess Instruments, Germany). The samples were rapidly heated from room temperature to 750 °C and held at 750 °C for 10 min, by such the content
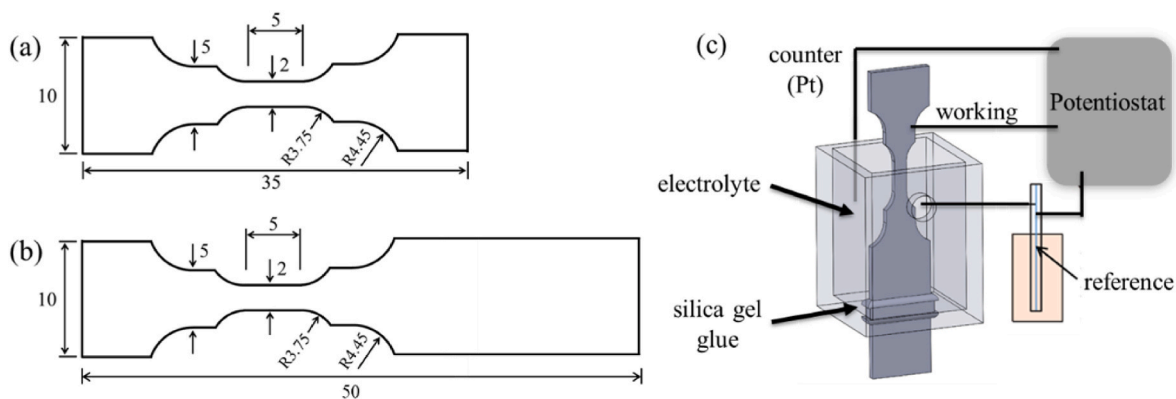
Table 1
Nominal composition of the studied X65 steel (in wt.%).

Elements	C	Si	Mn	P	S	Cu	Ni
wt.%	0.07	0.23	1.17	0.01	0.002	0.14	0.15
Elements	Mo	V	Nb	Ti	N	Al	Fe
wt.%	0.13	0.03	0.02	0.002	0.07	0.031	Bal.

Fig. 1. Geometry of the tensile test sample for (a) ex-situ and (b) in-situ hydrogen charging. (c) Schematic of the setup for in-situ hydrogen charging.

Table 2
Summary of testing conditions in this study.

Group	Testing condition	H condition	Strain rate
1	Vacuum in SEM	H-free	10^{-4} s^{-1}
		Ex-situ (12 h, −5 mA/cm^2)	10^{-4} s^{-1}
2	Air	H-free	10^{-3} s^{-1}
		Ex-situ (12 h, −5 mA/cm^2)	10^{-3} s^{-1}
3	In-situ H	Pre-charging (3 h, −5 mA/cm^2) + In-situ (−5 mA/cm^2)	10^{-4} s^{-1}
			10^{-3} s^{-1}
4	In-situ H Interrupted test	Pre-charging (3 h, −5 mA/cm^2) + In-situ (−5 mA/cm^2)	10^{-4} s^{-1}

of both diffusible and trapped hydrogen can be obtained.

3. Results

3.1. Microstructure analysis

Fig. 2 demonstrates the microstructure of the studied X65 carbon steel, which shows the ferrite matrix with heterogeneously distributed bainite. The details of each microconstituent are characterized by ECC images shown in Fig. 2b–c, where the ferrite phase exhibits a polygonal grain structure containing randomly distributed statistically stored dislocations. The bainite shows a different microstructure, where the lath-like ferrite phases are arranged in platelets with elongated cementite precipitated in between. Also, the normal direction-inverse pole figure (ND-IPF) map with the corresponding image quality (IQ) map are presented in Fig. 2d–e. Accordingly, the grain size of ferrite phase was determined as 8.8 μm, and the volume fraction of ferrite and bainite was calculated as 75.9% and 24.1%, respectively.
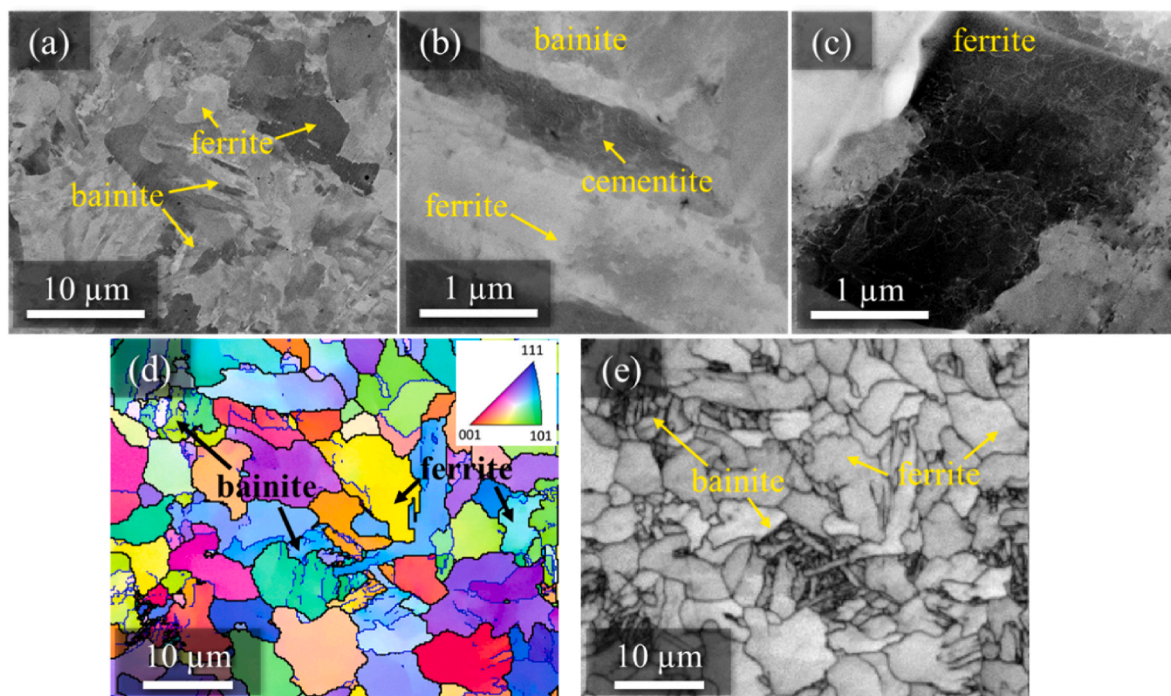

Fig. 2. Microstructure of tested X65 steel: BSE micrograph (a) of the matrix, ECC images showing the details of bainite (b) and ferrite (c), and IPF map (d) with the corresponding IQ map (e) [24].

3.2. Tensile test with ex-situ hydrogen charging

As mentioned in the experimental section, the first testing group was conducted in the vacuum condition inside the SEM chamber, where both hydrogen-free and ex-situ hydrogen charged samples were tested until fracture under a relatively slow strain rate. Fig. 3 shows the engineering stress-strain curves of this testing group, i.e., black solid line and black dashed line represent the hydrogen-free and ex-situ hydrogen charged condition, respectively. By comparison, the hydrogen shows a minor effect on both fracture elongation and strength. Specifically, for the hydrogen-free condition, the fracture elongation was 29.4%, the yield strength (YS) was 473.7 MPa, and the UTS was 563.7 MPa. When hydrogen was ex-situ pre-charged, the fracture elongation was reduced to 28.8%, and the YS and UTS were 478.8 and 570 MPa with 1.1% and 1.2% increment, respectively, compared to the hydrogen-free condition. Here, the hydrogen embrittlement factor (%HE) showing the level of hydrogen-induced mechanical degradation was adopted as [10]:

$$\%HE = 100\left(1 - \frac{\varepsilon_H}{\varepsilon_0}\right) \qquad (1)$$

where ε_H and ε_0 are the fracture elongation of hydrogen charged and uncharged samples, respectively. Hence, the %HE is in the scope between 0 and 1, where 0 means the sample is unaffected by hydrogen with no ductility loss, while 1 means the material is sensitive to hydrogen with a maximum extend. In terms of the tests that were conducted in vacuum, the %HE is only 2.0%. This minor hydrogen effect can also be observed from the tensile test videos, fracture gauge surface, and the fracture surface. The recorded videos are displayed in the supplementary document, where video 1 and 2 demonstrates the hydrogen-free and ex-situ hydrogen charged condition, respectively. The videos demonstrate a similar fracture behavior for both testing conditions including a uniform elongation, necking, and plastic fracture processes. From the fractured gauge surface shown in Fig. 4a and c, both cases show a pronounced necking with abundant plasticity, and no surface cracks can be observed on the surfaces. Moreover, the fracture surfaces, as demonstrated in Fig. 4b for hydrogen-free and Fig. 4d for hydrogen-pre-charged condition, manifest a pure ductile fracture behavior. In both cases, the fracture surface was covered with dimples with some inclusion-induced voids. Overall, hydrogen shows a negligible effect in the first testing group.

Since the studied carbon steel exhibits a high hydrogen diffusivity due to its Body Centered Cubic (BCC) structure, massive hydrogen loss
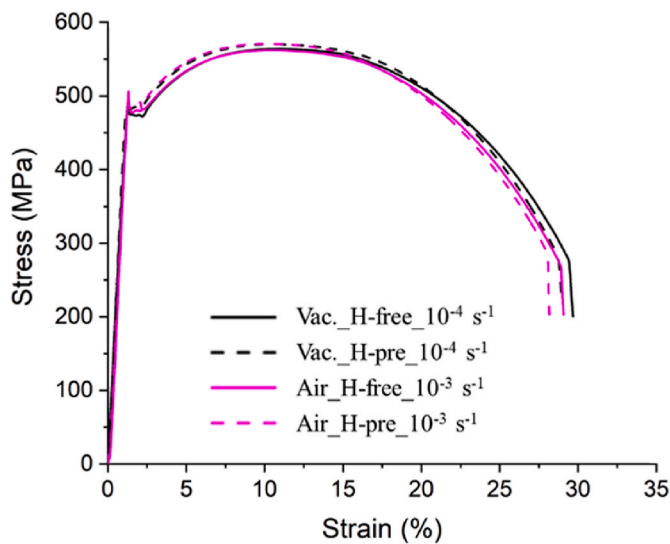
was expected after the sample was taken out from the electrolyte and during the straining process. To minimize the hydrogen outgassing, the second testing group was carried out in the air condition with a faster strain rate (10^{-3} s^{-1}). By such, the time for both preparation and test can be reduced. The engineering stress-strain curves for this testing group are presented in Fig. 3 as the purple solid line and purple dashed line, indicating the hydrogen-free and ex-situ hydrogen charged conditions, respectively. Similar to the results of the first testing group, a minor hydrogen effect is observed, though the overall testing time has been reduced to minimize the hydrogen loss. For the hydrogen-free sample tested in air condition, the fracture elongation is 28.9% and the YS and UTS are 477.6 and 562.1 MPa, respectively. For the sample with pre-charged hydrogen, the fracture elongation is 28.1% with a corresponding %HE of 2.8%. Moreover, the YS and UTS are 483.7 and 570.6 MPa, which is an increase of 1.3% and 1.5% compared to the hydrogen-free condition. Similar to the tests in vacuum, no clear hydrogen effect can be noticed from the fractured gauge surface and fracture surface. As shown in Fig. 5a and c, the gauge surface in both hydrogen-free and hydrogen-pre-charged conditions demonstrates a severe plastic deformation without any detectable surface cracks. The fracture surface shown in Fig. 5b and d exhibits a pure ductile fracture mode dominated by dimples. Although a hydrogen-induced strengthening and reduced fracture elongation can be found from the stress-strain curves, the difference is only 1–2% within the scatter and can be neglected. As a summary, both testing group 1 and 2 revealed no detectable brittle effect from hydrogen on the tested samples.

3.3. Tensile test with in-situ hydrogen charging

The above results indicate that ex-situ tests with the current pre-charging condition are unable to induce hydrogen-assisted fracture due to hydrogen loss after pre-charging. Hence, in-situ hydrogen charging, as shown in Fig. 1c, is a prerequisite to maintain a saturated and homogeneously distributed hydrogen throughout the test. By such, the hydrogen loss from the ex-situ charging process as for testing groups 1 and 2 can be avoided, and the hydrogen effect can be captured properly. The engineering stress-strain curves under in-situ hydrogen charging are shown as red lines in Fig. 6. In this testing condition, a clear hydrogen degradation effect on the mechanical properties is noticed. Regarding the tensile test with a 10^{-3} s^{-1} strain rate (red dashed line), the elongation is reduced to 24.2%, which indicates a %HE of 16.3%. The yield strength and UTS are 491.3 and 586.2 MPa, which is increased by 2.9% and 4.3% compared to the hydrogen-free condition, respectively. When the in-situ tensile test was performed with a 10^{-4} s^{-1} strain rate (red solid line), a more degradation effect can be found, where the fracture elongation is further reduced to 16.7% with a %HE of 43.2%. The corresponding YS and UTS are 489.1 and 585.9 MPa with an increment of 3.3% and 3.9% compared to the hydrogen-free condition under the same strain rate. A summary of the hydrogen effect on the mechanical properties in different testing conditions is exhibited in Table 3.

The effect of hydrogen can also be noticed from the fractured gauge surface and the fractography. For the first two testing groups, the fractured gauge surfaces show plastic deformation without any surface cracks and the fractographies are ductile fracture covered by dimples. For the tensile tests with in-situ hydrogen charging, massive secondary cracks can be observed on the gauge surface as shown in Fig. 7. In the higher strain rate condition (10^{-3} s^{-1} in Fig. 7b), the secondary cracks demonstrate large openings that merge into elongated cracks demonstrating severe plasticity due to the accelerated crack propagation process compared to the slow straining condition (10^{-4} s^{-1} in Fig. 7a). In addition, the fracture surfaces after in-situ charging tests exhibit a clear brittle behavior. As shown in Fig. 8, brittle fracture was observed in the edge region of the fracture surface, while in the center of the fracture surface, a mixture of brittle and void coalescence ductile fracture was observed. For the sample that was fractured with 10^{-4} s^{-1} loading rate,

Fig. 3. Engineering stress-strain curves of the studied steel under hydrogen-free and hydrogen ex-situ charged conditions in both vacuum and air environment.
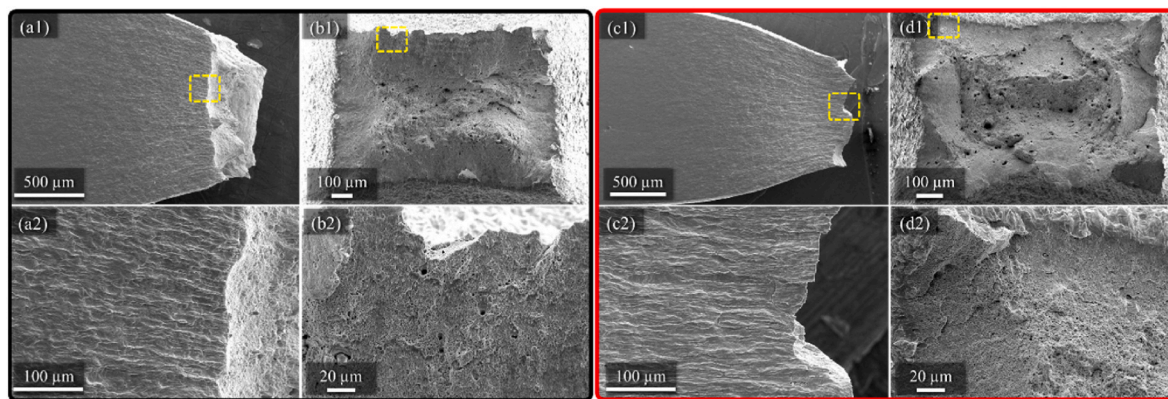
Fig. 4. Gauge surfaces (a, c) and fractographies (b, d) of the samples after loading to fracture in hydrogen-free (a1-b2) and pre-charged (c1-d2) conditions tested in the SEM vacuum chamber with 10^{-4} s^{-1} strain rate. (a2-d2) are the magnified images of the yellow dashed areas in (a1-d1). (For interpretation of the references to colour in this figure legend, the reader is referred to the Web version of this article.)
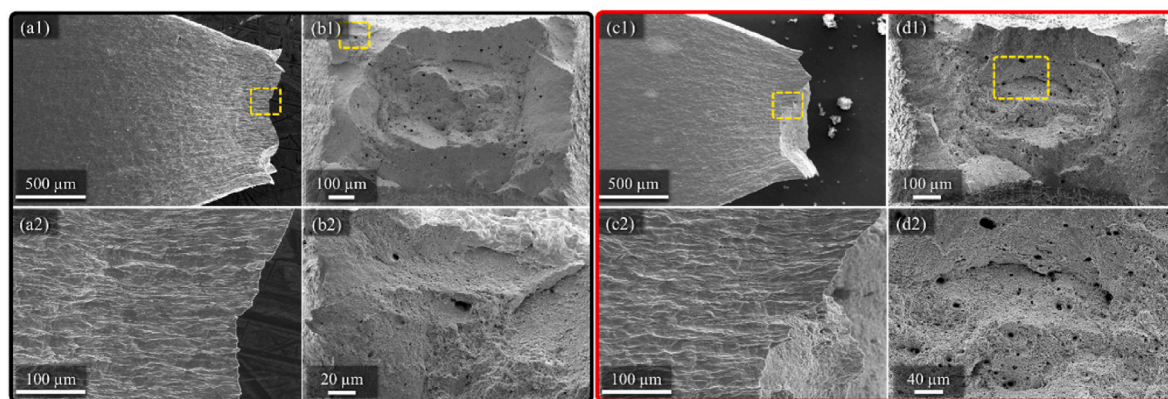

Fig. 5. Gauge surfaces (a, c) and fractographies (b, d) of the samples after loading to fracture in hydrogen-free (a1-b2) and hydrogen pre-charged (c1-d2) conditions tested in air with 10^{-3} s^{-1} strain rate. (a2-d2) are the magnified images of the yellow dashed areas in (a1-d1). (For interpretation of the references to colour in this figure legend, the reader is referred to the Web version of this article.)
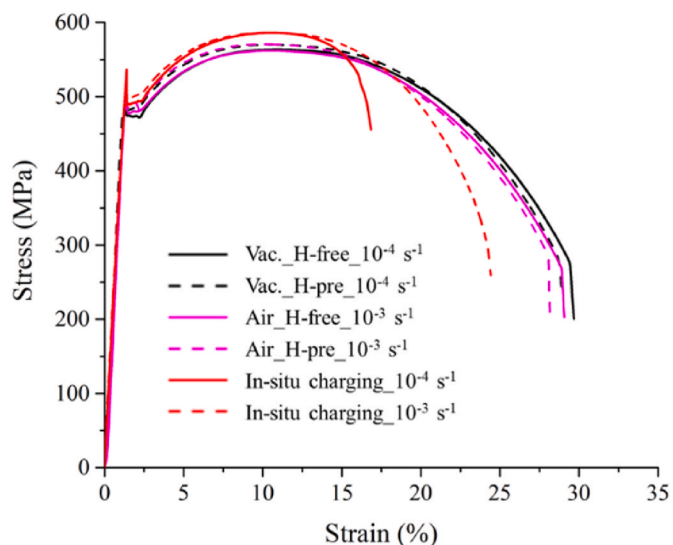

Fig. 6. Engineering stress-strain curves of studied sample under multiple conditions demonstrated in Fig. 3, plus additional testing under in-situ hydrogen charging condition.

Table 3
Summary of the mechanical properties.

Group	Testing condition	H condition	σ_y (MPa)	σ_{UTS} (MPa)	$\varepsilon_{frac.}$ (%)	Average %HE
1	Vacuum	H-free,10^{-4} s^{-1}	473.7 ± 6.2	563.7 ± 6.0	29.4 ± 0.2	–
		Ex-situ, 10^{-4} s^{-1}	478.8 ± 6.8	570.3 ± 7.2	28.8 ± 0.7	2.0
2	Air	H-free, 10^{-3} s^{-1}	477.6 ± 5.8	562.1 ± 7.1	28.9 ± 0.3	–
		Ex-situ, 10^{-3} s^{-1}	483.7 ± 7.4	570.6 ± 3.9	28.1 ± 0.5	2.8
3	In-situ H	In-situ, 10^{-4} s^{-1}	489.1 ± 4.1	585.9 ± 2.6	16.7 ± 1.2	43.2
		In-situ, 10^{-3} s^{-1}	491.3 ± 8.2	586.2 ± 5.5	24.2 ± 0.9	16.3

the brittle region close to the surface exhibits a mixture of cleavage and quasi-cleavage fracture morphologies, which appeared as either flat surface or river markings involved with plasticity near the tear ridges (Fig. 8(a3)). In particular, cleavage that initiated at a second phase particle and ended with a critical facet is highlighted by the red box. In contrast, for the sample that was tested at higher loading rate, a predominance of quasi-cleavage fracture was observed on the brittle region (Fig. 8(b3)).
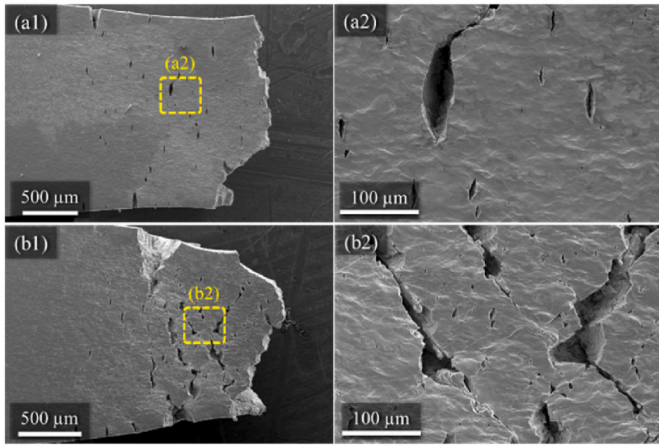
Fig. 7. SEM images of gauge surface cracks on the samples loaded to fracture under in-situ charging condition with 10^{-4} s^{-1} (a1-a2) and 10^{-3} s^{-1} (b1-b2) strain rates.

3.4. Interrupted tensile test with in-situ hydrogen charging

Though the secondary cracks can be observed on the fractured gauge surface under in-situ charging, the evolution of crack including initiation and propagation cannot be revealed clearly on the fractured sample due to the large crack opening angle and the severe plastic deformation around the cracks. Therefore, interrupted tensile tests were conducted to investigate the crack nucleation and propagation behavior, which can provide a key clue to understand the cracking mechanism. The in-situ interrupted tests were performed at 10^{-4} s^{-1} strain rate on four specimens, which were terminated at UTS, UTS+2% elongation, UTS+4% elongation, and at fracture. The SEM record of the gauge surface for each interrupted condition are presented in Fig. 9. At the UTS point with the maximum tensile strength, the gauge surface shows a relief morphology under uniform plastic deformation (Fig. 9a). No crack but some extruded inclusions can be observed on the surface. With 2% additional elongation, small cracks primarily formed inside the inclusions can be found on the gauge surface (Fig. 9b), With further straining up to UTS+4%

elongation, numerous secondary cracks perpendicular to the tensile direction were formed on the gauge surface (Fig. 9c). These formed cracks ended up with longer crack length, larger crack opening angle and an increased crack density on the gauge surface after fractured (Fig. 9d).

4. Discussion

4.1. Ex-situ vs. in-situ hydrogen charging

In the current study, the hydrogen effect on the samples was investigated via both ex-situ and in-situ charging methods. The results indicate a neglectable hydrogen effect under ex-situ charging, and a severe brittle effect under in-situ charging. Specifically, the ex-situ hydrogen charged sample exhibited a pure ductile fracture (Figs. 3 and 4), crack-free gauge surface (Fig. 5), and minor elongation reduction (Figs. 3 and 4). In contrast, the in-situ charged samples showed a brittle fracture surface (Fig. 8), multiple secondary cracks on the gauge surface (Fig. 7), and a noticeable elongation reduction (Fig. 6). To explain the contribution of hydrogen in different charging conditions, the corresponding hydrogen distribution needs to be presented. Therefore, a 2D diffusion model was built taking the four sides of gauge part into consideration to mimic a more accurate hydrogen distribution. The width and thickness direction of the sample gauge was set as the X axis from 0 to L_x and Y axis from 0 to L_y, respectively. Then Fick's 2nd law $\frac{\partial C}{\partial t} = D \frac{\partial^2 C}{\partial x^2}$ was applied. Here, the C denotes the hydrogen concentration, t is the time for hydrogen charging/discharging, and D is the diffusion coefficient set as 1.0×10^{-10} m^2/s [38]. The equation was solved numerically using the finite difference method [39], where the domain is first discretised by establishing a set of equally spaced mesh points for each variable:

$$x_i = i\Delta x, i = 0, ..., N_x \tag{2–1}$$

$$y_j = j\Delta y, j = 0, ..., N_y \tag{2-2}$$

$$t_n = i\Delta t, n = 0, ..., N_t \tag{2–3}$$

$C_{i,j}^n$ is introduced as the mesh function that approximates $C(x_i, y_i, t_n)$. Using the Forward Euler Scheme [39], the diffusion equation can be solved iteratively to obtain the concentration $C_{i,j}^{n+1}$ at each timestep as:
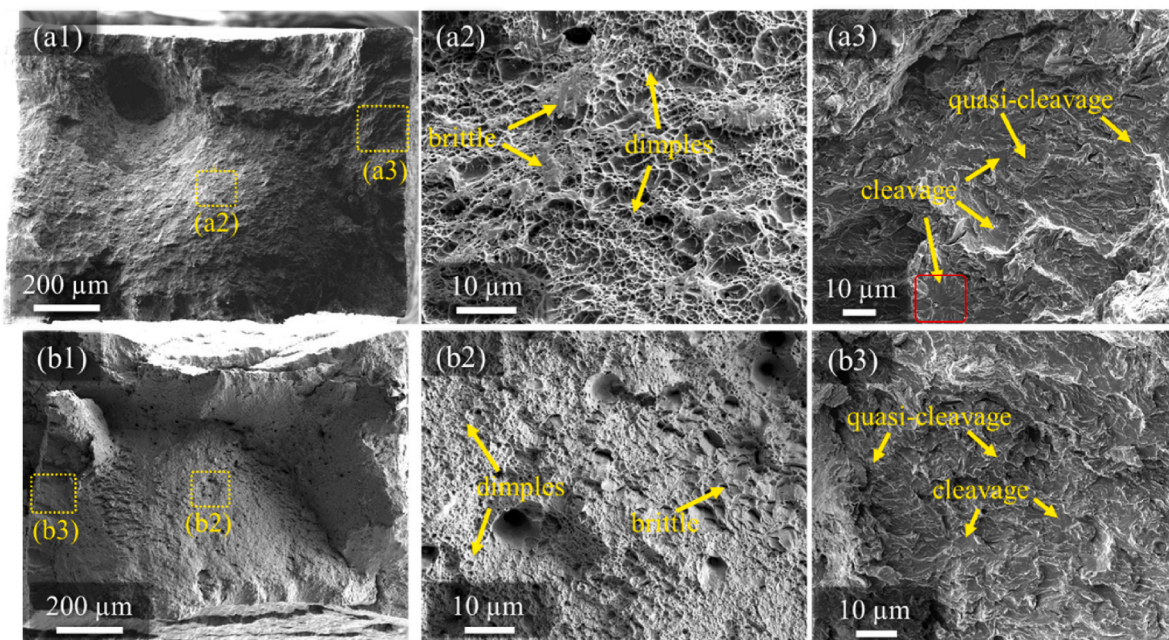

Fig. 8. Fractography of the test X65 steel after loading to fracture under in-situ hydrogen charging condition with 10^{-4} s^{-1} (a1-a3) and 10^{-3} s^{-1} (b1-b3) strain rate.
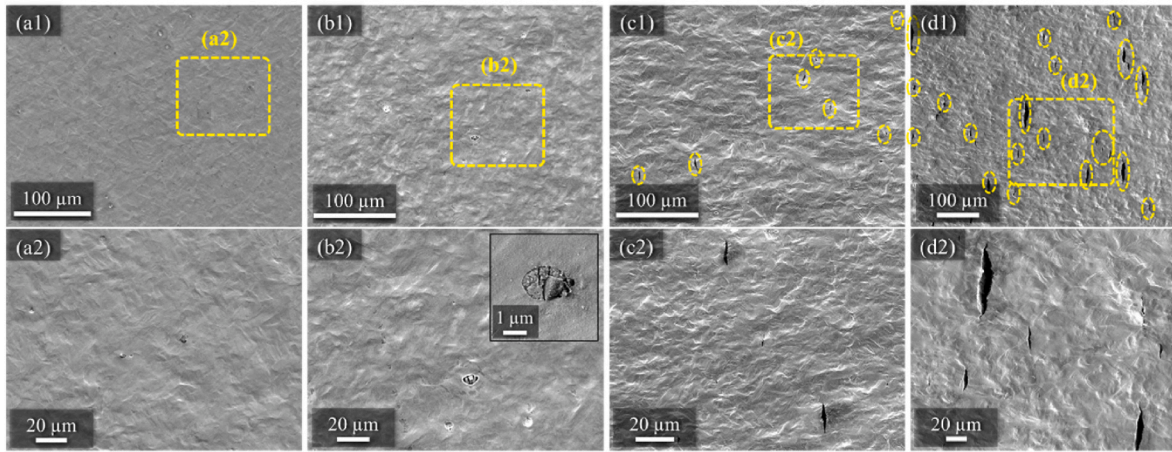
Fig. 9. Gauge surface after interrupted tensile test under in-situ hydrogen charging stopped at (a) UTS, (b) UTS+2% elongation, (c) UTS+4% elongation, and (d) fracture.

$$C_{i,j}^{n+1} = C_{i,j}^{n} + D\Delta t \left(\frac{C_{i+1,j}^{n} - 2C_{i,j}^{n} + C_{i-1,j}^{n}}{(\Delta x)^2} + \frac{C_{i,j+1}^{n} - 2C_{i,j}^{n} + C_{i,j-1}^{n}}{(\Delta y)^2} \right) \qquad (3)$$

By using the boundary and initial conditions summarized in Table 4, the hydrogen concentration in the 2D cross section of the gauge area can be calculated during the charging and discharging. In this work, the samples after ex-situ hydrogen charging were tested in two different conditions: inside SEM chamber with a slow strain rate and in air with a faster strain rate. The dwell times between the completion of hydrogen charging and the end of the tensile test were 60 and 10 min, respectively. Fig. 10 shows the hydrogen distribution on the gauge cross-sections after 3 h of charging (a) followed by 10 (b) and 60 min (c) of discharging. The edge of the hydrogen distribution indicates the boundary of the sample gauge area. After 3 h of charging, hydrogen was uniformly distributed in the sample. During the subsequent discharging process, a fast hydrogen depletion behavior was observed. After 10 min of discharging, the hydrogen concentration in the sample center was less than 50% and the remaining hydrogen content was less than 25%. After 60 min of discharging, however, only 1.7% of the total hydrogen remained in the sample. The massive hydrogen outgassing effect in the time lag between the end of charging and the tensile test was also confirmed, where the hot extraction was applied on three samples after 3 h charging in the same condition and with 0, 10, and 60 min of discharging time. The result shows a 0.444 wppm hydrogen dissolved in sample after charging, and the amount of dissolved hydrogen reduced to 0.204 and 0.08 wppm after 10 and 60 min of discharging, respectively. This rapid hydrogen loss was caused by the high hydrogen diffusivity in BCC structured carbon steel, which is proposed as the reason for the minor detrimental effect from ex-situ charging. Although there was still ~25% of hydrogen remaining in the sample during the fast strain rate ($10^{-3}\,\mathrm{s}^{-1}$) tensile test, the observed negligible hydrogen degradation effect indicates that a critical amount of hydrogen is necessary to initiate cracking. In contrast, the in-situ hydrogen charging method guarantees a constant high hydrogen concentration on the sample surface, which results in a severe hydrogen—defects interaction with noticeable mechanical property degradation as shown in Fig. 6. It is worth noting that some

microstructural defects can act as irreversible hydrogen trapping sites causing the hydrogen to be trapped instead of diffusing out during the discharging process. However, the comparison of the fracture surface, gauge surface and stress-strain curves indicate that the trapped hydrogen did not play a major role in the current study. Therefore, the in-situ charging is a more suitable method to investigate the hydrogen effect for the studied sample.

4.2. Crack initiation and propagation

Based on the interrupted tests shown in Fig. 9, secondary cracks begin to nucleate at UTS+2% elongation. The sample was further examined in detail focusing on the spots for crack initiation. In total, 105 secondary cracks were detected on the gauge surface, all of which were characterized by SEM. Interestingly, 93.3% of the cracks were associated with inclusions. Further EDS analysis was carried out to detect the composition and dimensions of the relevant inclusions. Two representative inclusions with their chemical compositions are illustrated in Fig. 11. It shows that all cracked inclusions are composed of manganese sulfide and aluminum oxide (MnS–Al_2O_3). Moreover, all the cracks are nucleated either on the MnS–Al_2O_3 interface or the inclusion—matrix interface.

It is well known that the stress states of the interfaces pertaining to different inclusions and the matrix are significantly affected by their relatively different physical properties and crystallographic features. Their corresponding physical properties are summarized in Table 5. The different thermal expansion coefficients between MnS and Al_2O_3 as well as the matrix and inclusions, in particular for MnS, would promote initiation of microvoids. Moreover, the significant difference in the hardness and Young's modulus can result in high residual stress along the interface. Hu et al. [32] calculated the residual stress at the interfaces around the inclusions in a X70 carbon steel, and demonstrated that the maximum residual stress at the interface of Al_2O_3—matrix and MnS—matrix are 2235 and 6261 MPa, respectively. Here, taking the geometry into account, the residual stress distribution was calculated around an inclusion using the ABAQUS finite element approach. The residual stress was estimated by considering the cooling from 655 °C tempering process to room temperature based on the thermal expansion coefficient difference (Table 5) between each inclusion and matrix. The results, shown in Fig. 11h, indicate a clear stress concentration at the interfaces between inclusions—matrix and different inclusions. Therefore, during the tensile test with in-situ hydrogen charging, hydrogen will be trapped and segregated at these interfaces owing to the super-abundant hydrogen on the surface. The accumulated hydrogen at the interfaces can reduce the cohesive energy as proposed by the HEDE

Table 4
Initial and boundary conditions used for solving the diffusion equation for the charging and discharging of hydrogen in a 2D cross section.

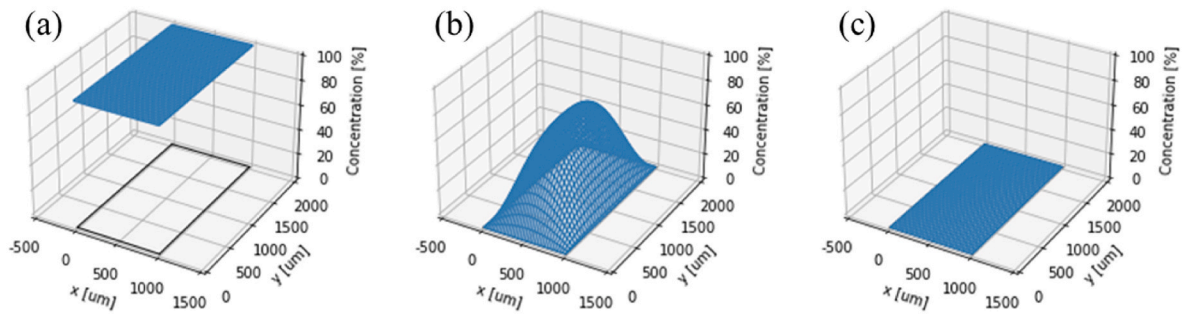|	Boundary conditions	Initial conditions
Charging	$C(0,0,t) = C(0,L_y,t) = C(L_x,0,t) = C(L_x, L_y,t) = 100$	$C(x,y,0) = 0$
Discharging	$C(0,0,t) = C(0,L_y,t) = C(L_x,0,t) = C(L_x, L_y,t) = 0$	$C(x,y,0) = C_{final\ charged\ stage}$

Fig. 10. Hydrogen distribution after (a) 3 h charging, followed by (b) 10 min and (c) 60 min of discharging, respectively.
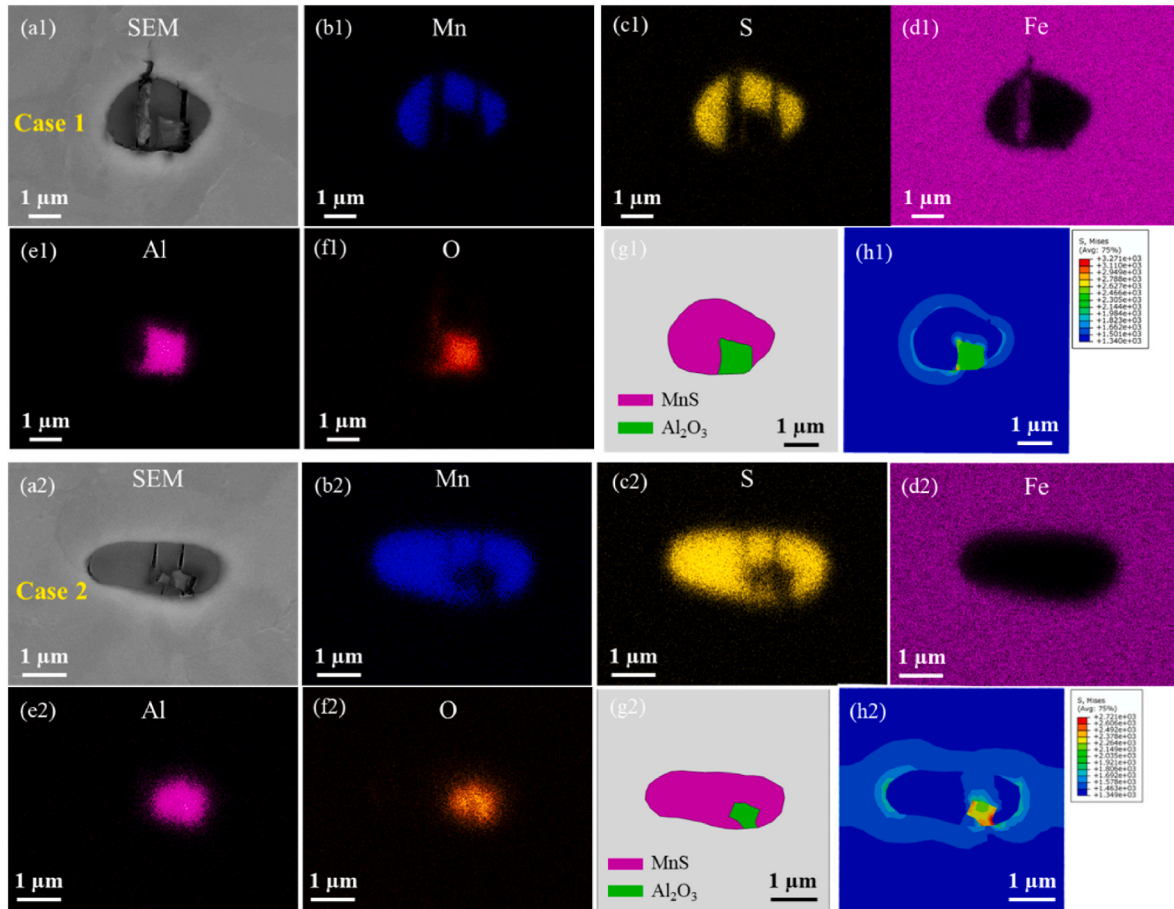

Fig. 11. Two cases of inclusions with the morphology (a), EDS mapping (b–g), and residual stress distribution (h).

Table 5
Physical properties of inclusions in the studied carbon steel [32,42–44].

Inclusion	Thermal expansion coefficient ($10^{-6}/°C$)	Vickers Hardness (GPa)	Young's modulus (GPa)
Al_2O_3	8.2	23	402
MnS	18.1	1.4	138
α-Fe matrix	10.8	1.57	207

mechanism. When the applied tensile stress exceeds the cohesive stress, cracks will initiate and propagate along these interfaces. Also, it has been reported that the segregated hydrogen leads to lattice expansion and therefore enhances the internal stress at the interfaces [40,41]. As a result, these interfaces are the "vulnerable spots" for crack initiation under the hydrogen effect. Once the crack initiates, it can propagate either transgranularly towards the matrix or along the interface depending on the local stress condition and the crystallographic relations.

To investigate the propagation path of secondary cracks in the matrix, the gauge surface of the fractured sample under in-situ charging was analyzed by EBSD. Two examples of EBSD IPF maps exhibiting secondary cracks are demonstrated in Fig. 12. It clearly shows that all the secondary cracks grow in a transgranular manner along the perpendicular direction to the tensile axis. Moreover, the {110} traces of the corresponding grains along the crack path are marked in the EBSD maps. Here, the marked yellow traces coincide most signicantly with the cracking path. As can be seen, all the cracks grow along the {110} specific low-index plane, which is the potential slip plane for the BCC-structured materials. Similar {110} dominated slip plane cracking
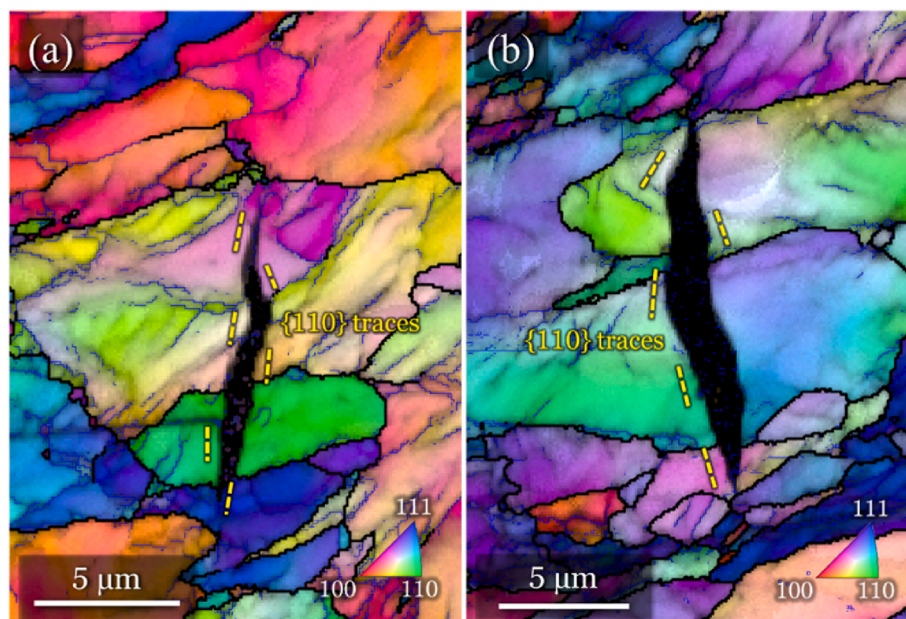
Fig. 12. Inverse pole figures (IPFs) of gauge surface containing secondary cracks from interrupted test stopped at UTS+4% (a) and fracture (b–c).

behavior was also reported by the previous studies [45,46]. Nakasato and Bernstein performed a crystallographic study on the cracks induced by hydrogen charging on a purified iron, and they claimed that the cracks follow a {110}-type plane [45]. Additionally, the molecular dynamics study was carried out to examine the hydrogen effect on crack propagation in α-Fe [46]. The result indicated that hydrogen accumulation on slip planes could decrease the surface energy and promoted the slip planes separation, leading to the fracture occurred at {110} slip planes. However, a different hydrogen-induced crack propagation behavior in BCC materials was also reported, where the cracks grew along the {100} cleavage plane [47,48]. Moreover, the hydrogen induced crack growth behavior along the combined {110}, {100}, and {112} planes has also been documented [45,49,50]. Two possible reasons for the different cracking behavior are the different alloying elements and the different hydrogen concentration. It has been reported that the cracks always follow the {110} slip plane in pure iron, while the cracks shift to the {100} plane in a Fe–3%Si under the same testing condition. It was proposed that adding silicon can lower the cohesive energy of the close packed {110} plane in the scope of the HEDE mechanism or restrict the cross slip and enhance localized stress concentration according to the HELP mechanism [45]. Moreover, the crack along the {100} plane was clearly detected in pure iron in 0.7 MPa hydrogen, whereas the crack parallel to {110} plane was observed when the pressure was increased to 90 MPa [49]. This indicates that higher hydrogen concentration promotes highly localized slip band on the {110} planes with an escalated internal stress, facilitating the formation of cracks along those slip planes.

5. Conclusions

In this study, the hydrogen effect on X65 carbon steel was investigated by tensile tests using ex-situ and in-situ cathodic hydrogen charging methods. By comparing the hydrogen effect on the mechanical properties from different testing conditions using the post-mortem SEM, EBSD, and EDS characterizations, the following conclusions can be drawn:

1. When the ex-situ hydrogen charging method was applied, the hydrogen showed a minor effect resulting in a negligible fracture elongation reduction, dimple-dominated fracture surface, and crack-

free gauge surface. In contrast, significate degradation was detected during in-situ hydrogen charging, where a clear fracture elongation reduction, brittle fracture surface, and multiple secondary cracks on the gauge surface were observed. The relative high diffusivity of hydrogen in the studied BCC-structured material led to hydrogen depletion from ex-situ method, where the intrinsic hydrogen effect cannot be fully revealed. While the in-situ charging maintained a constant hydrogen concentration at the sample surface, promoting crack initiation and propagation at the surface. Therefore, the in-situ charging is a more suitable method for investigating hydrogen effect on steels analogous to X65 carbon steel.
2. During the in-situ tensile test, secondary cracks were observed on the gauge surface. The majority of the cracks initiated around the non-metallic MnS–Al$_2$O$_3$ inclusions, either on the interfaces between different inclusions or the interfaces between inclusion and matrix. This is due to the synergistic effect of the elevated stress concentration and the trapped hydrogen that locally promotes crack initiation and propagation.
3. The secondary cracks propagated in a transgranular manner, through both ferrite and bainite. The crystallographic analysis revealed that the cracks grow along typical {110} slip planes. Such cracking morphology is caused by the highly localized slip bands and high-pressure stress from dissolved hydrogen on {110} planes, facilitating the local crack propagation.

CRediT authorship contribution statement

D. Wang: Conceptualization, Methodology, Formal analysis, Data curation, Writing – original draft. **A.B. Hagen:** Formal analysis, Methodology, Writing – review & editing. **P.U. Fathi:** Formal analysis, Writing – review & editing. **M. Lin:** Formal analysis, Writing – review & editing. **R. Johnsen:** Formal analysis, Writing – review & editing. **X. Lu:** Formal analysis, Methodology, Conceptualization, Writing – review & editing.

Declaration of competing interest

The authors declare that they have no known competing financial interests or personal relationships that could have appeared to influence the work reported in this paper.

Data availability

Data will be made available on request.

Acknowledgements

Appendix A. Supplementary data

Supplementary data to this article can be found online at https://doi.org/10.1016/j.msea.2022.144262.

References

[1] T.N. Veziroglu, 21st century's energy: hydrogen energy system, in: J.W. Sheffield, Ç. Sheffield (Eds.), Assessment of Hydrogen Energy for Sustainable Development, Springer Netherlands, Dordrecht, 2007, pp. 9–31.

[2] J.O. Abe, A.P.I. Popoola, E. Ajenifuja, O.M. Popoola, Hydrogen energy, economy and storage: review and recommendation, Int. J. Hydrogen Energy 44 (29) (2019) 15072–15086.

[3] W.H. Johnson, On some remarkable changes produced in iron and steel by the action of hydrogen and acids, Proc. Roy. Soc. Lond. 23 (1874) 168–179.

[4] B. Sun, D. Wang, X. Lu, D. Wan, D. Ponge, X. Zhang, Current challenges and opportunities toward understanding hydrogen embrittlement mechanisms in advanced high-strength steels: a review, Acta Metall. Sin. 34 (2021) 741–754.

[5] R.A. Oriani, P.H. Josephic, Equilibrium aspects of hydrogen-induced cracking of steels, Acta Metall. 22 (9) (1974) 1065–1074.

[6] A.R. Troiano, The role of hydrogen and other interstitials in the mechanical behavior of metals, Metallogr. Microstruct. Anal. 5 (6) (2016) 557–569.

[7] C. Beachem, A new model for hydrogen-assisted cracking (hydrogen "embrittlement"), Metall. Mater. Trans. B 3 (2) (1972) 441–455.

[8] H.K. Birnbaum, P. Sofronis, Hydrogen-enhanced localized plasticity-a mechanism for hydrogen-related fracture, Mat. Sci. Eng. Struct. 176 (1) (1994) 191–202.

[9] P. Ferreira, I. Robertson, H. Birnbaum, Hydrogen effects on the interaction between dislocations, Acta Mater. 46 (5) (1998) 1749–1757.

[10] T. Depover, K. Verbeken, The detrimental effect of hydrogen at dislocations on the hydrogen embrittlement susceptibility of Fe-C-X alloys: an experimental proof of the HELP mechanism, Int. J. Hydrogen Energy 43 (5) (2018) 3050–3061.

[11] A. Metsue, A. Oudriss, X. Feaugas, Trapping/detrapping kinetic rates of hydrogen around a vacancy in nickel and some consequences on the hydrogen-vacancy clusters thermodynamic equilibrium, Comput. Mater. Sci. 151 (2018) 144–152.

[12] M. Nagumo, Hydrogen related failure of steels - a new aspect, Mater. Sci. Tech. Lond 20 (8) (2004) 940–950.

[13] R.B. McLellan, Z.R. Xu, Hydrogen-induced vacancies in the iron lattice, Scripta Mater. 36 (10) (1997) 1201–1205.

[14] H. Yu, A. Cocks, E. Tarleton, Discrete dislocation plasticity HELPs understand hydrogen effects in bcc materials, J. Mech. Phys. Solid. 123 (2019) 41–60.

[15] M.B. Djukic, G.M. Bakic, V. Sijacki Zeravcic, A. Sedmak, B. Rajicic, The synergistic action and interplay of hydrogen embrittlement mechanisms in steels and iron: localized plasticity and decohesion, Eng. Fract. Mech. 216 (2019), 106528.

[16] M.B. Djukic, V. Sijacki Zeravcic, G.M. Bakic, A. Sedmak, B. Rajicic, Hydrogen damage of steels: a case study and hydrogen embrittlement model, Eng. Fail. Anal. 58 (2015) 485–498.

[17] E. Ohaeri, U. Eduok, J. Szpunar, Hydrogen related degradation in pipeline steel: a review, Int. J. Hydrogen Energy 43 (31) (2018) 14584–14617.

[18] L. Ligang, X. Hong, L. Qiang, L. Yu, L. Peishuai, Y. Zhiqiang, Y. Hui, Evaluation of the fracture toughness of X70 pipeline steel with ferrite-bainite microstructure, Mater. Sci. Eng., A 688 (2017) 388–395.

[19] C. Zhou, B. Ye, Y. Song, T. Cui, P. Xu, L. Zhang, Effects of internal hydrogen and surface-absorbed hydrogen on the hydrogen embrittlement of X80 pipeline steel, Int. J. Hydrogen Energy 44 (40) (2019) 22547–22558.

[20] N.E. Nanninga, Y.S. Levy, E.S. Drexler, R.T. Condon, A.E. Stevenson, A.J. Slifka, Comparison of hydrogen embrittlement in three pipeline steels in high pressure gaseous hydrogen environments, Corrosion Sci. 59 (2012) 1–9.

[21] T. Depover, K. Verbeken, Hydrogen trapping and hydrogen induced mechanical degradation in lab cast Fe-C-Cr alloys, Mater. Sci. Eng., A 669 (2016) 134–149.

[22] E.S. Drexler, A.J. Slifka, R.L. Amaro, N. Barbosa, D.S. Lauria, L.E. Hayden, D. G. Stalheim, Fatigue crack growth rates of API X70 pipeline steel in a pressurized hydrogen gas environment, Fatig. Fract. Eng. Mater. Struct. 37 (5) (2014) 517–525.

[23] P. Fassina, F. Brunella, L. Lazzari, G. Re, L. Vergani, A. Sciuccati, Fatigue behavior of pipeline steel under hydrogen environment and low temperature, Procedia Eng. 10 (2011) 3345–3352.

[24] D. Wang, A.B. Hagen, D. Wan, X. Lu, R. Johnsen, Probing hydrogen effect on nanomechanical properties of X65 pipeline steel using in-situ electrochemical nanoindentation, Mater. Sci. Eng., A 824 (2021), 141819.

[25] L. Zhang, W. Cao, K. Lu, Z. Wang, Y. Xing, Y. Du, M. Lu, Effect of the cathodic current density on the sub-surface concentration of hydrogen in X80 pipeline steels under cathodic protection, Int. J. Hydrogen Energy 42 (5) (2017) 3389–3398.

[26] Y. Ogawa, M. Hino, M. Nakamura, H. Matsunaga, Pearlite-driven surface-cracking and associated loss of tensile ductility in plain-carbon steels under exposure to high-pressure gaseous hydrogen, Int. J. Hydrogen Energy 46 (9) (2021) 6945–6959.

[27] D. Hardie, E.A. Charles, A.H. Lopez, Hydrogen embrittlement of high strength pipeline steels, Corrosion Sci. 48 (12) (2006) 4378–4385.

[28] M.A. Mohtadi-Bonab, J.A. Szpunar, L. Collins, R. Stankievech, Evaluation of hydrogen induced cracking behavior of API X70 pipeline steel at different heat treatments, Int. J. Hydrogen Energy 39 (11) (2014) 6076–6088.

[29] L. Zhang, H. Shen, K. Lu, W. Cao, Y. Sun, Y. Fang, Y. Xing, Y. Du, M. Lu, Investigation of hydrogen concentration and hydrogen damage on API X80 steel surface under cathodic overprotection, Int. J. Hydrogen Energy 42 (50) (2017) 29888–29896.

[30] V. Singh, R. Singh, K.S. Arora, D.K. Mahajan, Hydrogen induced blister cracking and mechanical failure in X65 pipeline steels, Int. J. Hydrogen Energy 44 (39) (2019) 22039–22049.

[31] M. Fernandes, N. Cheung, A. Garcia, Investigation of nonmetallic inclusions in continuously cast carbon steel by dissolution of the ferritic matrix, Mater. Char. 48 (4) (2002) 255–261.

[32] H. Xiao, F. Huang, Z. Peng, L. Fan, J. Liu, Sequential kinetic analysis of the influences of non-metallic inclusions on hydrogen diffusion and trapping in high-strength pipeline steel with Al-Ti deoxidisation and Mg treatment, Corrosion Sci. 195 (2022), 110006.

[33] M. Asadipoor, A. Pourkamali Anaraki, J. Kadkhodapour, S.M.H. Sharifi, A. Barnoush, Macro- and microscale investigations of hydrogen embrittlement in X70 pipeline steel by in-situ and ex-situ hydrogen charging tensile tests and in-situ electrochemical micro-cantilever bending test, Mater. Sci. Eng., A 772 (2020), 138762.

[34] E.V. Chatzidouros, V.J. Papazoglou, D.I. Pantelis, Hydrogen effect on a low carbon ferritic-bainitic pipeline steel, Int. J. Hydrogen Energy 39 (32) (2014) 18498–18505.

[35] Y.-H. Lee, H.M. Lee, Y.-i. Kim, S.-H. Nahm, Mechanical degradation of API X65 pipeline steel by exposure to hydrogen gas, Met. Mater. Int. 17 (3) (2011) 389–395.

[36] D. Wang, X. Lu, D. Wan, X. Guo, R. Johnsen, Effect of hydrogen on the embrittlement susceptibility of Fe-22Mn-0.6C TWIP steel revealed by in-situ tensile tests, Mater. Sci. Eng., A 802 (2020), 140638.

[37] X. Lu, D. Wang, Effect of hydrogen on deformation behavior of Alloy 725 revealed by in-situ bi-crystalline micropillar compression test, J. Mater. Sci. Technol. 67 (2021) 243–253.

[38] Y.F. Cheng, Analysis of electrochemical hydrogen permeation through X-65 pipeline steel and its implications on pipeline stress corrosion cracking, Int. J. Hydrogen Energy 32 (9) (2007) 1269–1276.

[39] S. Linge, H.P. Langtangen, Diffusion Equations, Springer International Publishing, 2017, pp. 207–322.

[40] D. Wang, X. Lu, D. Wan, Z. Li, A. Barnoush, In-situ observation of martensitic transformation in an interstitial metastable high-entropy alloy during cathodic hydrogen charging, Scripta Mater. 173 (2019) 56–60.

[41] X. Lu, D. Wang, D. Wan, Z.B. Zhang, N. Kheradmand, A. Barnoush, Effect of electrochemical charging on the hydrogen embrittlement susceptibility of Alloy 718, Acta Mater. 179 (2019) 36–48.

[42] P. Juvonen, Effects of Non-metallic Inclusions on Fatigue Properties of Calcium Treated Steels, Helsinki University of Technology, 2004.

[43] C.H. Leung, L.H. Van Vlack, SOLUTION AND PRECIPITATION HARDENING IN (Ca, MN) SULFIDES AND SELENIDES, Metall. Trans. A 12 A (6) (1981) 987–991.

[44] L. Wang, N. Karimi, T. Sutardi, M.C. Paul, Numerical modelling of unsteady transport and entropy generation in oxy-combustion of single coal particles with varying flow velocities and oxygen concentrations, Appl. Therm. Eng. 144 (2018) 147–164.

[45] F. Nakasato, I.M. Bernstein, Crystallographic and fractographic studies of hydrogen- induced cracking in purified iron and iron- silicon alloys, Metall. Trans. A 9 (9) (1978) 1317–1326.

[46] R. Matsumoto, S. Taketomi, S. Matsumoto, N. Miyazaki, Atomistic simulations of hydrogen embrittlement, Int. J. Hydrogen Energy 34 (23) (2009) 9576–9584.

[47] D. Birenis, Y. Ogawa, H. Matsunaga, O. Takakuwa, J. Yamabe, Ø. Prytz, A. Thøgersen, Interpretation of hydrogen-assisted fatigue crack propagation in BCC iron based on dislocation structure evolution around the crack wake, Acta Mater. 156 (2018) 245–253.

[48] J. Hou, X.-S. Kong, C.S. Liu, J. Song, Hydrogen clustering in bcc metals: atomic origin and strong stress anisotropy, Acta Mater. 201 (2020) 23–35.

[49] D. Birenis, Y. Ogawa, H. Matsunaga, O. Takakuwa, J. Yamabe, Ø. Prytz, A. Thøgersen, Hydrogen-assisted crack propagation in α-iron during elasto-plastic fracture toughness tests, Mater. Sci. Eng., A 756 (2019) 396–404.

[50] E.D. Merson, P.N. Myagkikh, V.A. Poluyanov, D.L. Merson, A. Vinogradov, Quasi-cleavage hydrogen-assisted cracking path investigation by fractographic and side surface observations, Eng. Fract. Mech. 214 (2019) 177–193.